

Article

Design of Battery Thermal Management System with Considering the Longitudinal and Transverse Temperature Difference

Junhao Dong¹, Xipo Lu¹, Yang Sun¹, Vladislav Mitin^{1,2}, Huaping Xu¹ and Wei Kong^{1,*} ¹ School of Energy and Power, Jiangsu University of Science and Technology, Zhenjiang 212003, China² School of Mechanics and Energy, Mordovia State University, 430005 Saransk, Russia

* Correspondence: wkong@just.edu.cn

Abstract: For a bottom-liquid-cooled battery thermal management system (BTMS), the small contact area between the battery bottom and the cold plate leads to a large temperature difference in the battery height direction. In addition, the increase in coolant temperature from the inlet to the outlet results in an excessive temperature difference in the battery module in the coolant flow direction. In order to solve the above issues, a wavy channel was first designed to strengthen the heat exchange between the battery bottom and the cold plate. The maximum battery module temperature for the wavy-channel design is 29.61 °C, which is a reduction of 1.75 °C compared to the straight-channel design. Then, the transverse temperature difference in the battery module was reduced by introducing a composite-channel design. Finally, on the basis of the composite channel, phase change material (PCM) was added to the battery's top surface to reduce the temperature difference in the battery height direction. The results show that the maximum temperature and maximum temperature difference in the battery module of the composite-channel/PCM design proposed in this study are reduced by 6.8% and 41%, respectively, compared with the conventional straight-channel design.

Keywords: BTMS; wavy channel; composite channel; phase change material; temperature uniformity



Citation: Dong, J.; Lu, X.; Sun, Y.; Mitin, V.; Xu, H.; Kong, W. Design of Battery Thermal Management System with Considering the Longitudinal and Transverse Temperature Difference. *Energies* **2022**, *15*, 7448. <https://doi.org/10.3390/en15197448>

Academic Editor:
Djaffar Ould-Abdeslam

Received: 25 August 2022
Accepted: 6 October 2022
Published: 10 October 2022

Publisher's Note: MDPI stays neutral with regard to jurisdictional claims in published maps and institutional affiliations.



Copyright: © 2022 by the authors. Licensee MDPI, Basel, Switzerland. This article is an open access article distributed under the terms and conditions of the Creative Commons Attribution (CC BY) license (<https://creativecommons.org/licenses/by/4.0/>).

1. Introduction

To better control the maximum temperature and temperature uniformity of lithium-ion batteries, a large number of scholars have proposed various battery thermal management systems (BTMSs) [1–3]. Based on different cooling methods, BTMSs mainly involve air cooling [4,5], liquid cooling [6,7], phase change material cooling [8] and coupled cooling [9–11], which are implemented in various ways. Liquid cooling is widely applied due to its good cooling effect and high technological maturity [12]. Figure 1 shows that the liquid-cooled BTMS mainly includes the battery and the cold plate, in which the arrangement of the cold plate mainly comes in two forms. One is the cold plate placed between two batteries, which is defined as the side-liquid-cooled BTMS. The other is the cold plate placed on the bottom of the battery module, which is defined as the bottom-liquid-cooled BTMS.

In recent years, many researchers have reported on the side-liquid-cooled BTMS. Rao et al. [13] proposed a mini-channel cold plate. The influence of the inlet mass flow rate, flow direction, channel number and channel width on the battery temperature was investigated. The results indicated that the battery temperature can be well controlled with five channels. Considering that a rise in the coolant temperature in the flow direction leads to a decrease in its heat transfer capacity, Rao et al. [14] further developed a wedge-shaped channel to improve the heat transfer performance of the downstream channel. By investigating parameters such as the aspect ratio of the outlet, the inlet flow rate and the branching structure, it was found that the wedge-shaped channel possesses good cooling efficiency and temperature uniformity. To reduce the maximum battery temperature difference (ΔT_{\max}) and the pressure drop simultaneously, the authors of [15] designed a

divergent-shaped-channel cold plate, with the cross-sectional area of the channel increasing in the flow direction. The downstream flow velocity is reduced, while the heat transfer of the downstream channel is enhanced, thus reducing the flow resistance. To further reduce the battery temperature difference, Sheng et al. [16] reported a serpentine channel cold plate with a dual inlet and outlet. The results showed that the channel width has a greater effect on the temperature uniformity and system energy consumption and a smaller effect on the maximum battery temperature.

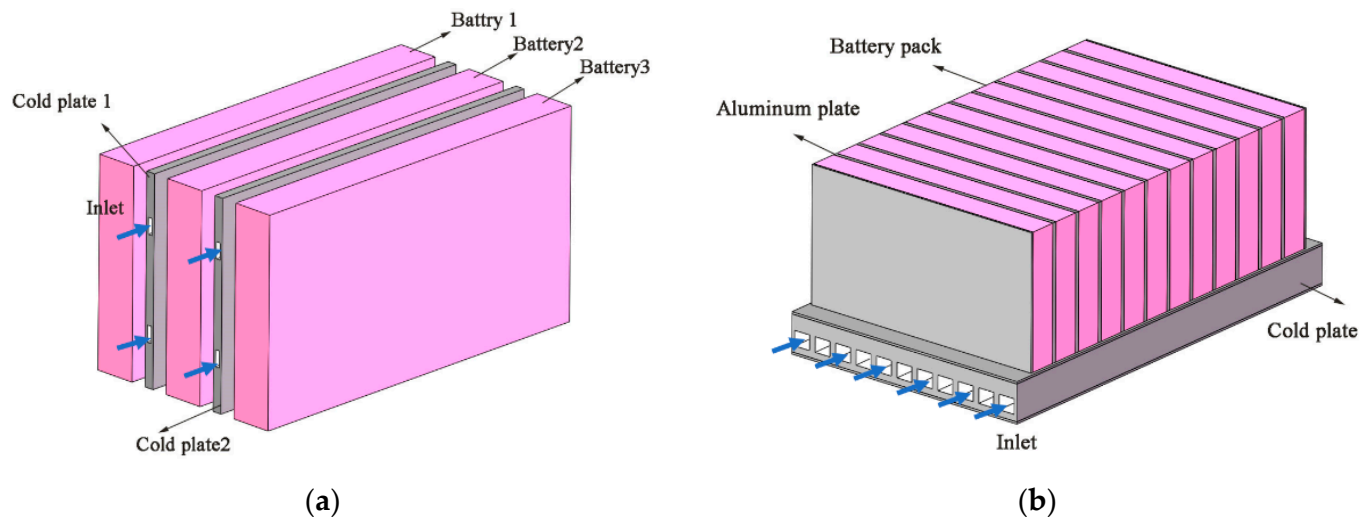


Figure 1. Schematic diagram of (a) the side-liquid-cooled BTMS; (b) the bottom-liquid-cooled BTMS.

Many scholars have also investigated the thermal performance of battery modules based on the side-liquid-cooled BTMS. Deng et al. [17] investigated the thermal performance of a battery module consisting of four batteries and five cold plates under 3 C and 5 C discharges. It was discovered that the middle battery was hotter, and more heat dissipation channels should be provided. Ding et al. [18] studied a BTMS with rectangular and circular flow channels. The results indicated that a lower T_{\max} was achieved using a rectangular channel. Xu et al. [19] analyzed the difference between U-shaped channels and serpentine channels. The results suggested that the serpentine channel performed better in reducing the maximum temperature difference in the battery module. In the case of a 3 C discharge, the ΔT_{\max} of the battery was 3.74 °C, which was 0.26 °C smaller than that of the U-shaped channel.

The battery's side area is several times larger than its bottom area, resulting in a much higher heat transfer efficiency between the battery and the cold plate in a side-liquid-cooled BTMS than in a bottom-liquid-cooled BTMS. However, the cold plate is placed between two batteries, so there is a potential battery safety issue caused by coolant leakage. The bottom-liquid-cooled BTMS effectively avoids this issue, is safer and has been practically applied in vehicles such as GM Bolt, BMW i3 and Rongwei ERX5. The bottom-liquid-cooled BTMS has meanwhile gained a lot of attention from researchers. Xu et al. [20] designed a cold plate with splitters. Five structural factors of the splitters were investigated using orthogonal experiments. Chung et al. [21] reported that the large thermal resistance in the height direction of the battery was one of the main factors that hindered the efficient heat dissipation of the battery. In response to the large temperature difference in large battery modules, Chen et al. [6] proposed a parallel bi-directional microchannel cold plate for large battery modules, which reduced the temperature difference and energy consumption of the module by 52% and 82%, respectively, compared with the conventional structure. Li et al. [22] proposed a U-shaped liquid-cooled BTMS with heat pipes, which utilizes heat pipes to export the accumulated heat inside the battery module and cool it uniformly through a cold plate. Compared to the cold plate without heat pipes, the average battery

module temperature was decreased by 7.66%, and the maximum temperature difference was reduced by 73.02%.

The profile of the channel significantly affects the cooling performance of the cold plate. Therefore, to enhance the heat dissipation capacity of the conventional straight channel, numerous novel channel designs have been proposed, such as leaf-like channels [23–26], tree-like channels [27,28], topological channels [29,30] and spiral channels [31,32]. Although the advantages of these novel channel designs have been demonstrated in terms of reducing the maximum battery temperature and improving the battery temperature uniformity, from the application point of view, these novel channel designs are quite complex, which increases the cost and creates some obstacles to practical application. As a result, the conventional straight channel is used more widely in the literature.

However, the bottom-liquid-cooled BTMS design has the following two issues. On the one hand, the small area of the battery bottom limits the heat exchange efficiency between the battery and the cold plate, resulting in a large temperature difference in the height direction of the battery. On the other hand, the large temperature difference between the coolant inlet and outlet leads to an excessive temperature difference in the battery module in the coolant flow direction. In this study, a wavy-channel cold plate is proposed in order to reduce the maximum temperature of the battery module and to strengthen the heat exchange between the battery and the cold plate. Compared with the above-mentioned channel designs, the wavy channel is simple, making its practical application easy. In order to reduce the temperature difference in the battery module in the direction of coolant flow, a composite channel was designed. Finally, on the basis of the composite channel, phase change material (PCM) was added to the top of the battery to further reduce the temperature difference in the battery height direction.

2. Model

2.1. Geometry

The model geometry includes the battery, aluminum plate and cold plate. As the part marked by the yellow dashed line in Figure 2a, a repetitive unit was selected as the calculation domain in this study due to the symmetry. Figure 2b,c show the schematic diagrams of the conventional straight channel and the wavy channel, respectively. The detailed dimensions of the wavy channel are shown in Figure 2d. The model parameters are shown in Table 1. In addition, the batteries are labeled as 1 to 12 in order along the direction of coolant flow, as shown in Figure 2d.

Table 1. Model parameters [33,34].

Parameters	PCM (RT27)	Battery	Aluminum	Coolant
Specific heat capacity ($\text{J kg}^{-1} \text{K}^{-1}$)	2400 (Solid Phase) 1800 (Liquid Phase)	1633	871	4182
Thermal conductivity ($\text{W m}^{-1} \text{K}^{-1}$)	0.24 (Solid Phase) 0.15 (Liquid Phase)	29/29/1	202.4	0.6
Density (kg m^{-3})	870 (Solid Phase) 760 (Liquid Phase)	2136.8	2719	998.2
Viscosity of liquid phase ($\text{kg m}^{-1} \text{s}^{-1}$)	0.00324			0.001003
Latent heat of phase change of PCM ($\text{J kg}^{-1} \text{K}^{-1}$)	179,000			
Phase change temperature ($^{\circ}\text{C}$)	28			
Phase change interval ($^{\circ}\text{C}$)	2			

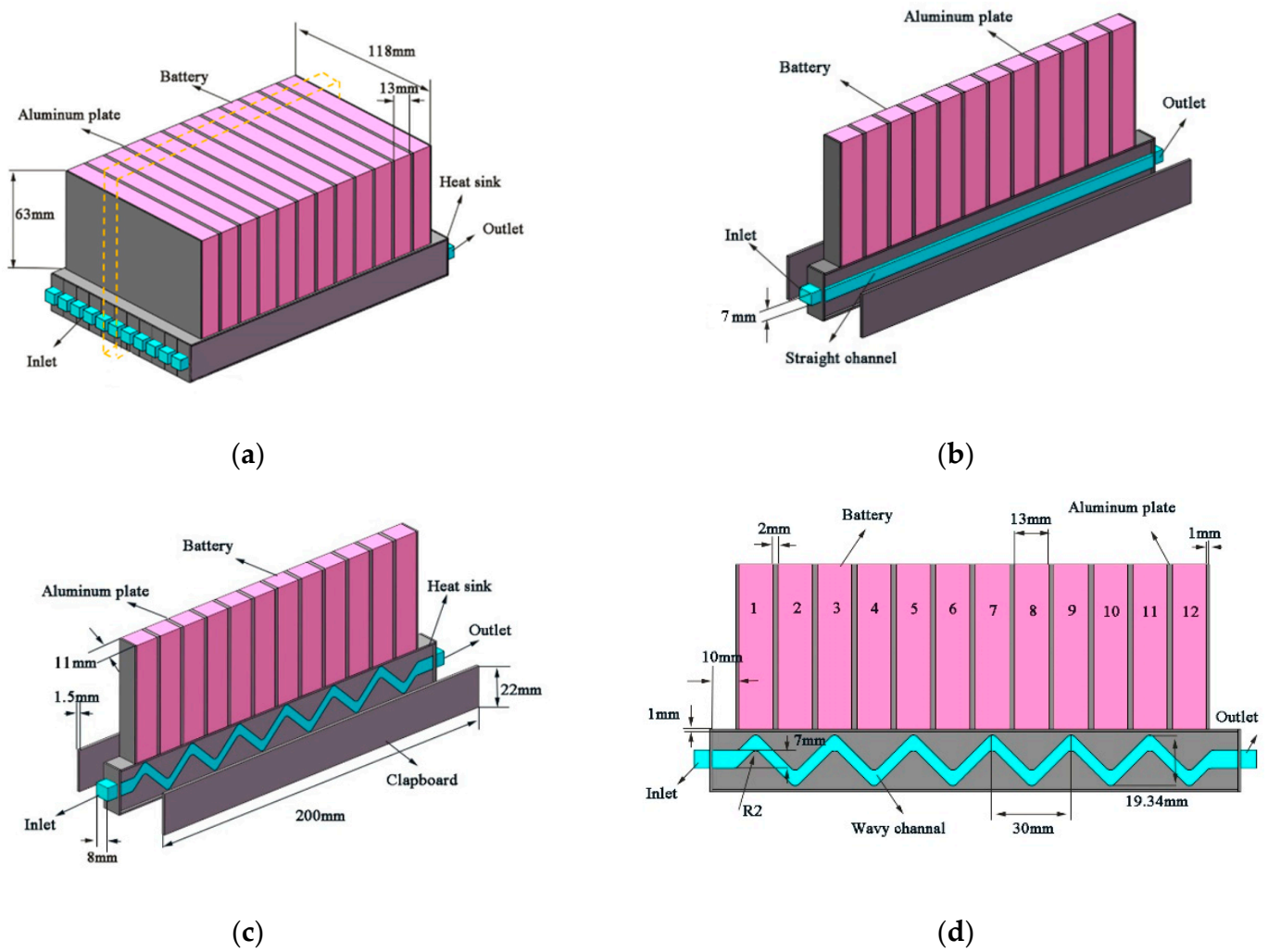


Figure 2. Liquid-cooled BTMS: (a) overall view; (b) straight channel; (c) wavy channel; (d) detailed dimensions of wavy channel.

2.2. Equations and Boundary Conditions

Based on the coolant inlet rate, density, viscosity and characteristic length, the Reynolds number is 133, which is much less than 2300. Therefore, the laminar flow model was used for the coolant region [35].

The equations in the coolant region are:

Continuity equation:

$$\frac{\partial \rho_w}{\partial t} = \nabla \cdot (\rho_w \vec{v}_w) \quad (1)$$

Momentum equation:

$$\rho_w \frac{\partial \vec{v}_w}{\partial t} + \rho_w (\vec{v}_w \cdot \nabla) \vec{v}_w = -\nabla p_w + \mu_w \nabla^2 \vec{v}_w \quad (2)$$

Energy conservation equation:

$$\rho_w C_{p,w} \frac{\partial T_w}{\partial t} + \nabla \cdot (\rho_w C_{p,w} \vec{v}_w T_w) = \nabla \cdot (k_w \nabla T_w) \quad (3)$$

where ρ_w , $C_{p,w}$, T_w , μ_w and k_w in the above equation represent the density (kg m^{-3}), specific heat capacity ($\text{J kg}^{-1} \text{K}^{-1}$), temperature (K), kinetic viscosity ($\text{pa}\cdot\text{s}$) and thermal

conductivity ($\text{W m}^{-1} \text{K}^{-1}$) of the coolant, respectively. v_w represents the velocity vector of the coolant.

The equation of energy conservation in the battery region is:

$$\rho_{bat} C_{p,bat} \frac{\partial T}{\partial t} = k_{bat} \nabla^2 T_{bat} + q \quad (4)$$

where ρ_{bat} , $C_{p,bat}$, $C_{p,bat}$ and T_{bat} in the above equation are the density (kg m^{-3}), specific heat capacity ($\text{J kg}^{-1} \text{K}^{-1}$), thermal conductivity ($\text{W m}^{-1} \text{K}^{-1}$), and temperature (K) of the battery, respectively. q (W m^{-3}) is the heat source of the battery.

The analysis of heat transfer processes in the PCM region uses the enthalpy-porosity method [36]:

$$\frac{\partial(\rho_{pcm} H_{pcm})}{\partial t} + \nabla \cdot (\rho_{pcm} \vec{u} H_{pcm}) = k_{pcm} \nabla^2 T_{pcm} \quad (5)$$

$$H_{pcm} = h_0 + \int_{T_0}^T C_{p,pcm} dT + \beta \gamma \quad (6)$$

where ρ_{pcm} , k_{pcm} , T_{pcm} , H_{pcm} and γ represent the density, thermal conductivity, temperature, enthalpy (J) and latent heat of phase change ($\text{J kg}^{-1} \text{K}^{-1}$) of the PCM, respectively. h_0 and $C_{p,pcm}$ represent the reference enthalpy and the specific heat capacity of the PCM, respectively. In addition, since the thermal properties of the PCM are largely determined by its state, the liquid-phase volume (β) can be given as follows:

$$\begin{cases} \beta = 0 & T_{pcm} \leq T_s \\ \beta = 1 & T_{pcm} \geq T_l \\ \beta = \frac{T_{pcm} - T_s}{T_l - T_s} & T_s < T_{pcm} < T_l \end{cases} \quad (7)$$

where T_s and T_l represent the onset and termination temperatures of the phase transition of the PCM, respectively. In addition, the natural convection of the phase change material is described by the continuity equation and the momentum equation [36].

$$\nabla \cdot (\rho \vec{u}) = 0 \quad (8)$$

$$\frac{\partial(\rho \vec{u})}{\partial t} + \nabla \cdot (\rho \vec{u} \vec{u}) = -\nabla p + \nabla \cdot \tau + \rho_\alpha [1 - \zeta(T - T_0)] \vec{g} + \frac{(1 - \beta)^2}{\beta^2 + 0.001} A_{mush} \vec{u} \quad (9)$$

In the above equation, τ is the stress tensor, ρ_α represents the density of the PCM at ambient temperature, ζ is the coefficient of thermal expansion with a value of 0.0008161K^{-1} , and A_{mush} is the fuzzy region constant with a value of 105.

The energy equation for the aluminum plate region is represented by the following equation:

$$\rho_{al} C_{p,al} \frac{\partial T_{al}}{\partial t} = k_{al} \nabla^2 T_{al} \quad (10)$$

where ρ_{al} , $C_{p,al}$, k_{al} and T_{al} in the above equation are the density (kg m^{-3}), specific heat capacity ($\text{J kg}^{-1} \text{K}^{-1}$), thermal conductivity ($\text{W m}^{-1} \text{K}^{-1}$) and temperature (K) of the aluminum plate, respectively.

The initial temperature of each component of the model is set to 25°C . The inlet temperature is 25°C . The coolant flow rate at the inlet is set to 1g/s , and the direction is perpendicular to the inlet boundary. The boundary equation between the components can be expressed as follows:

$$-k_w \frac{\partial T_w}{\partial n} = -k_{bat} \frac{\partial T_{bat}}{\partial n} = -k_i \frac{\partial T_i}{\partial n} \quad (11)$$

2.3. Model Validation

In this study, Fluent was used to build the above model. The SIMPLE algorithm and second-order windward format were selected to solve the model [37]. The relaxation factor was the default value, and the standard initialization method was adopted to initialize the model. In addition, in order to verify the grid independence, five models with different numbers of grids were built, as shown in Table 2. The effect of the number of grids on the results is illustrated in Figure 3. As shown in Figure 3, when the grid number is increased from 2,524,904 to 3,041,312, the changes in T_{gmax} and ΔT_{gmax} of the battery module are less than 0.2%. Therefore, a grid number of 2,524,904 meets the accuracy requirement, and the grid parameter setting was adopted for the other models. To further verify the accuracy of the model, a model was established using the parameters reported in Reference [34], as shown in Table 1. The discharge rate was 2.5 C, and the initial temperature of the model was 25 °C. All boundaries were adiabatic. The calculated data agreed with the measured data, and the error remained within 5%, as shown in Figure 4, which proves the accuracy of the model.

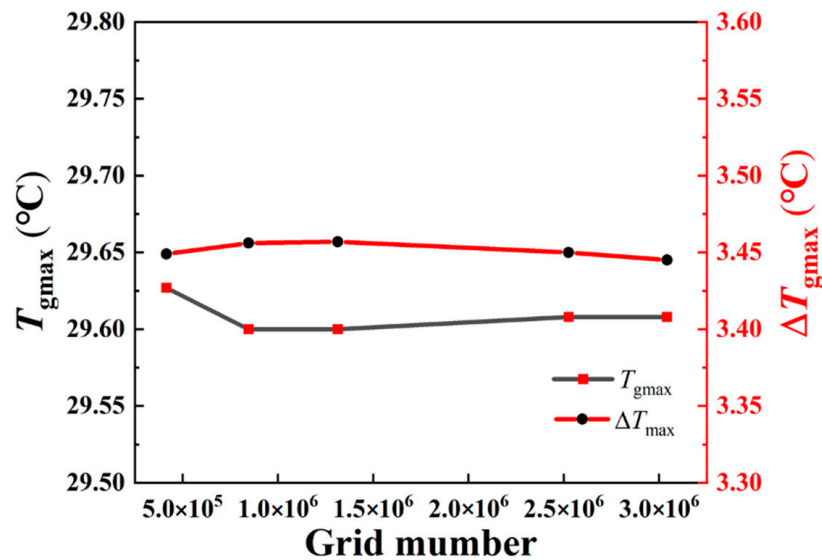


Figure 3. Grid independence verification.

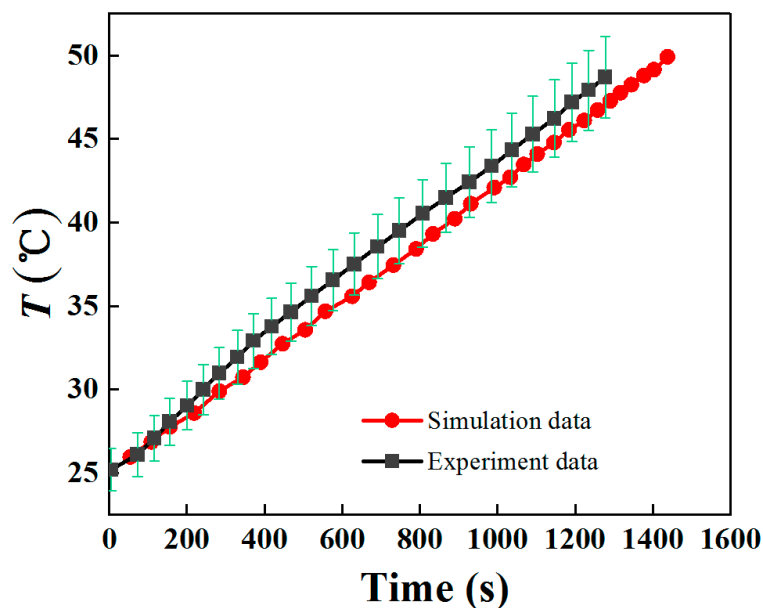


Figure 4. Model verification (with 5% error bars) [34].

Table 2. Grid independence verification.

	Mesh 1	Mesh 2	Mesh 3	Mesh 4	Mesh 5
Number of meshes	414640	845958	1313585	2524904	3041312

3. Results and Discussion

3.1. Wavy-Channel Design

Figure 5 shows the temperature distribution of the battery module. It is obvious that the temperature distributions of the two designs are similar. The lowest temperature is located at the bottom of battery 1 near the coolant inlet, and the highest temperature appears at the top of battery 12 near the coolant outlet. In addition, the maximum battery module temperature T_{gmax} for the wavy-channel design is 29.61 °C, a reduction of 1.75 °C compared to the straight-channel design. The reason is that, on the one hand, the wavy channel increases the heat transfer area between the coolant and the cold plate, which in turn enhances the cooling performance of the cold plate. On the other hand, as shown in Figure 6, it is difficult to transfer heat to the center of the straight channel due to the large heat resistance of the boundary layer. For the wavy channel, when the coolant flows along the channel, the secondary flow (Dean vortex) is generated due to the centrifugal force, which promotes the mixing of hot and cold fluids in the channel and strengthens the heat transfer.

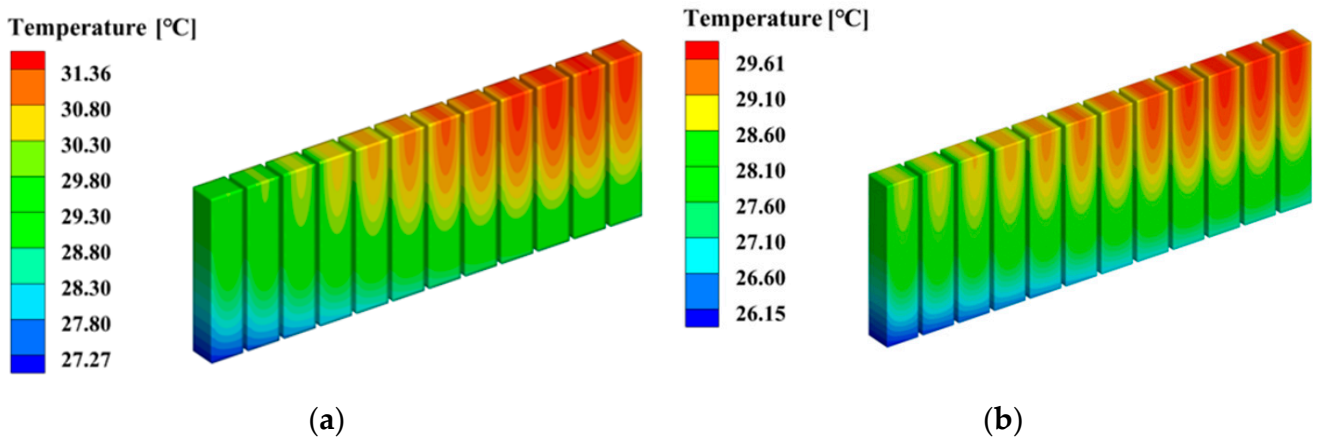


Figure 5. Temperature distribution of battery module: (a) straight channel and (b) wavy channel.

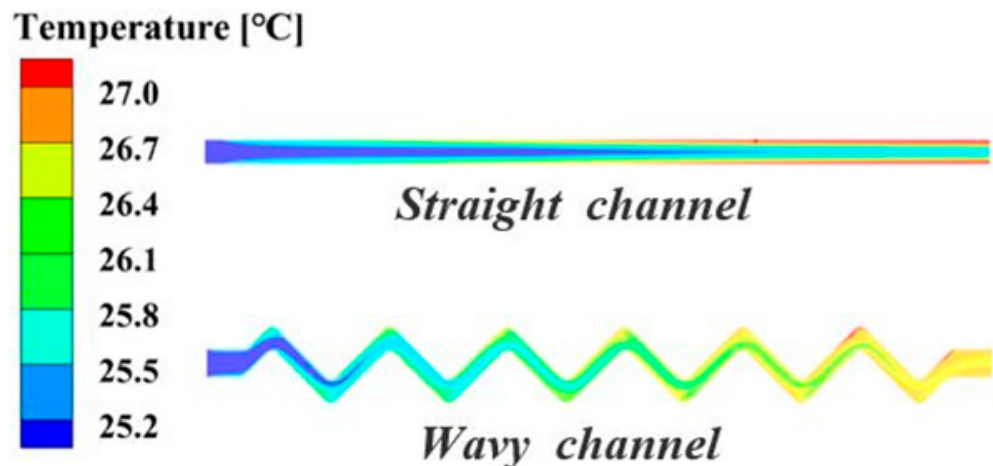


Figure 6. Temperature distribution of central section of channel.

Figure 7 compares the ΔT_{max} and T_{max} of each battery for the two designs. It is clear that the T_{max} of each battery with the wavy-channel design is lower than that of

the straight-channel design. For example, the T_{\max} of battery 1 near the inlet of the wavy-channel design is 28.86 °C, which is 1.16 °C lower than that of the straight-channel design. In addition, it can be found that the T_{\max} of the battery gradually increases along the coolant flow direction. For instance, the T_{\max} of battery 1 near the inlet is 28.67 °C, while the T_{\max} of battery 12 near the outlet is 29.59 °C. In terms of ΔT_{\max} , the difference in ΔT_{\max} between the two designs is not significant. The ΔT_{\max} values for battery 1, battery 6 and battery 12 are 2.54 °C, 2.51 °C and 2.45 °C for the straight-channel design, respectively, which are 2.46 °C, 2.42 °C and 2.44 °C for the wavy-channel design, respectively.

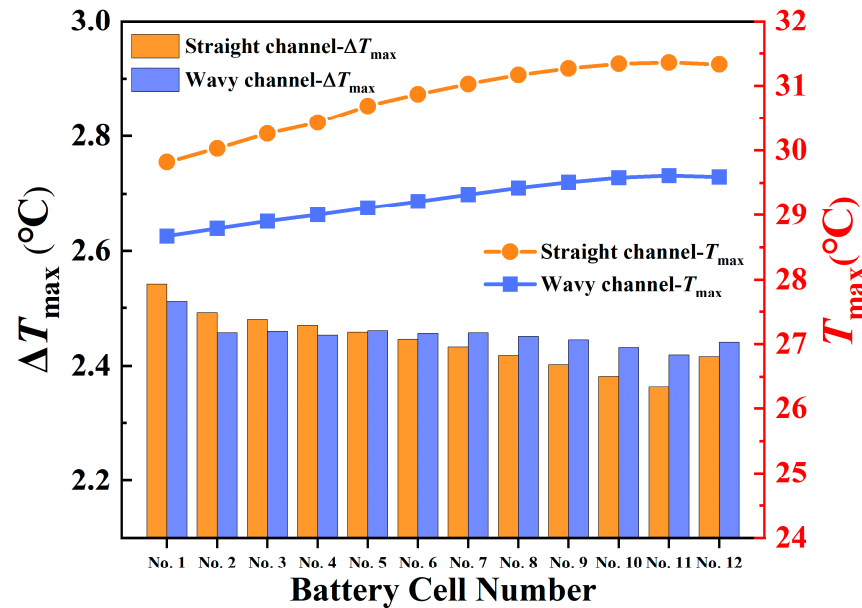


Figure 7. The maximum temperature difference (ΔT_{\max}) and maximum temperature (T_{\max}) of each battery.

3.2. Composite-Channel Design

For the wavy-channel design, the temperature inhomogeneity of the battery module is mainly reflected in two directions: the height direction of the battery, which is defined as the longitudinal temperature difference, and the flow direction of the coolant, which is defined as the transverse temperature difference. Because the coolant temperature is lowest at the inlet, the minimum temperature of the battery module occurs near the coolant inlet region. To improve the minimum temperature of the battery module, a composite-channel design is proposed, as shown in Figure 8. The front end of the composite channel is a straight channel, and the rear end is a wavy channel, where the straight-channel length is denoted by d . To study the effect of straight-channel length, models with d of 31 mm, 46 mm and 61 mm were developed and are described in this section.

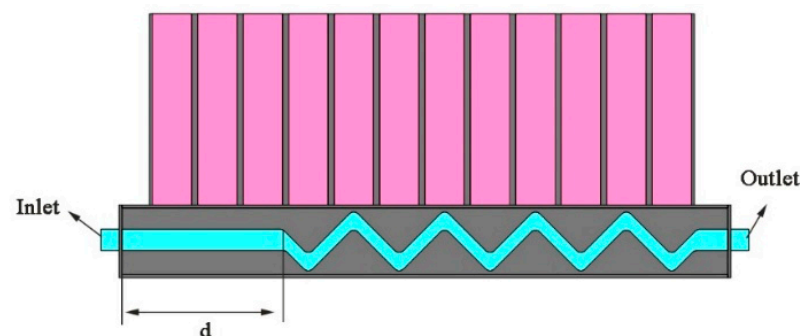


Figure 8. Schematic diagram of composite channel.

As shown in Figure 9, as the straight-channel length d increases, the maximum temperature of the battery near the inlet gradually increases. When d increases from 31 mm to 61 mm, the maximum temperature of battery 1 increases from 29.04 °C to 29.39 °C, as shown in Figure 10b. This is due to the fact that the heat transfer capacity of the straight channel is weaker than that of the wavy channel, so the longer the straight channel, the worse the cooling effect of the battery near the inlet region. In addition, as shown in Figure 10, the temperature uniformity between batteries increases as d increases. When $d = 61$ mm, the difference between the lowest temperatures T_{\min} of battery 1 and battery 12 is 0.39 °C, which is much smaller than 1.03 °C for the wavy channel, and the difference between the maximum temperatures T_{\max} of battery 1 and battery 12 is 0.26 °C, which is much smaller than 0.94 °C for the wavy channel.

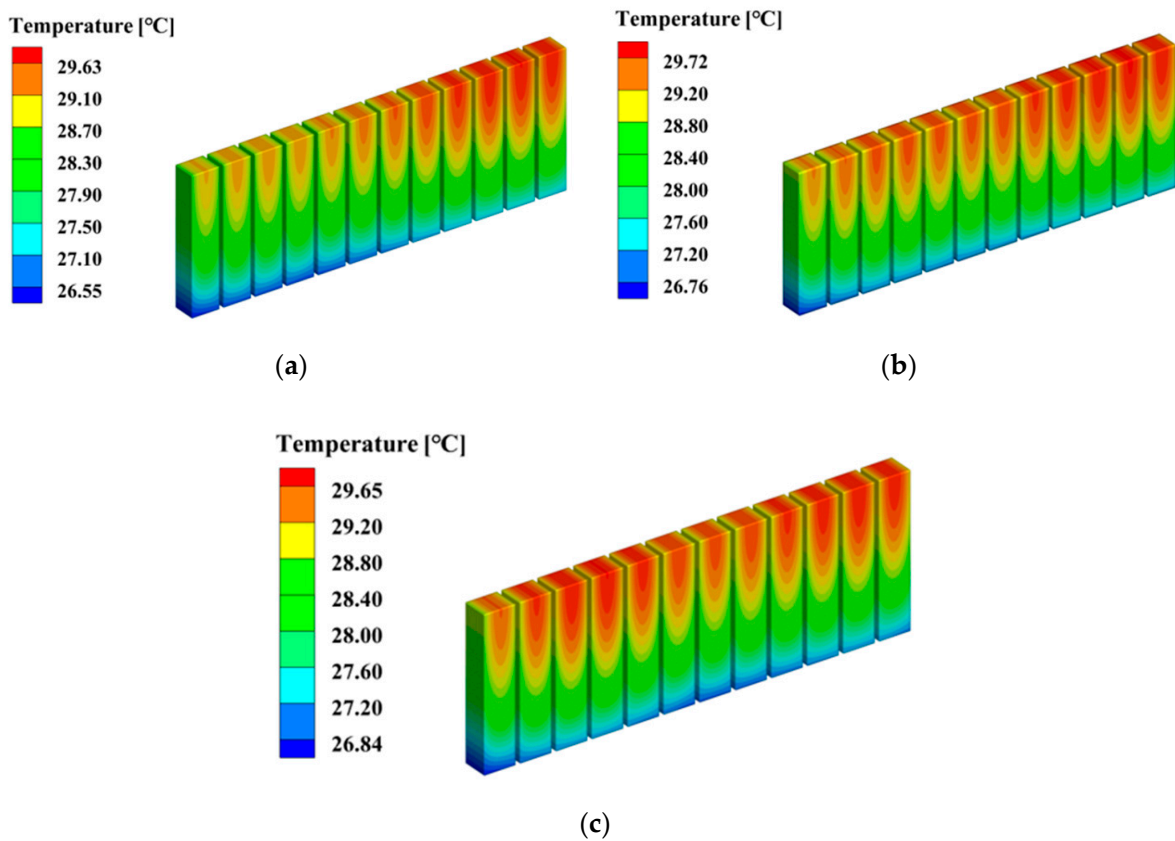


Figure 9. Temperature distribution of battery module: (a) $d = 31$ mm; (b) $d = 46$ mm; (c) $d = 61$ mm.

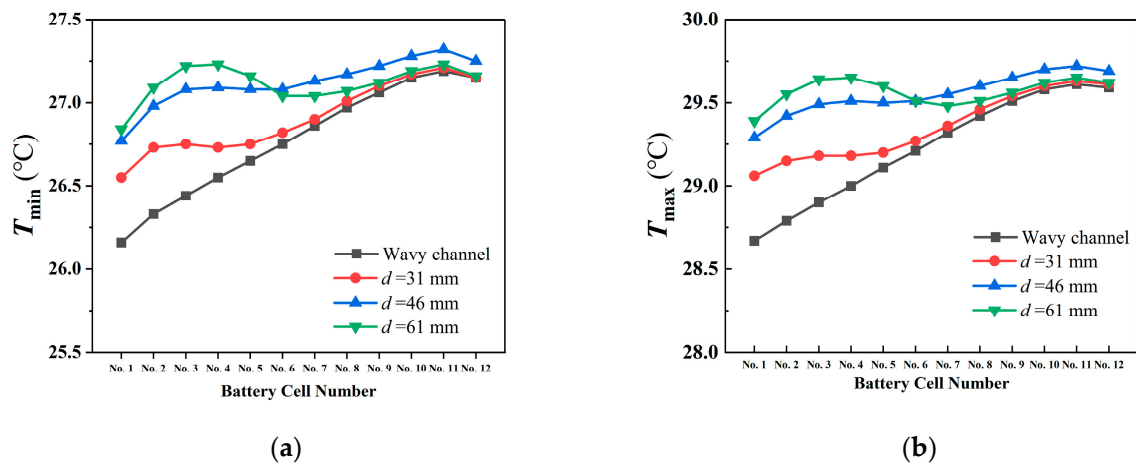


Figure 10. Temperature of each battery under different configurations: (a) T_{\min} and (b) T_{\max} .

Figure 11 presents the variation in the maximum temperature T_{gmax} and the maximum temperature difference ΔT_{gmax} of the battery module. On the one hand, ΔT_{gmax} decreases continuously as the value of d increases. ΔT_{gmax} is only 2.81 °C for the $d = 61$ mm composite channel, which is 0.65 °C less than the 3.46 °C of the wavy channel. On the other hand, the straight-channel length in the composite channel has a negligible effect on the maximum temperature of the battery module. Therefore, the composite-channel design significantly improves the temperature uniformity of the battery module, and the recommended straight-channel length d is 61 mm.

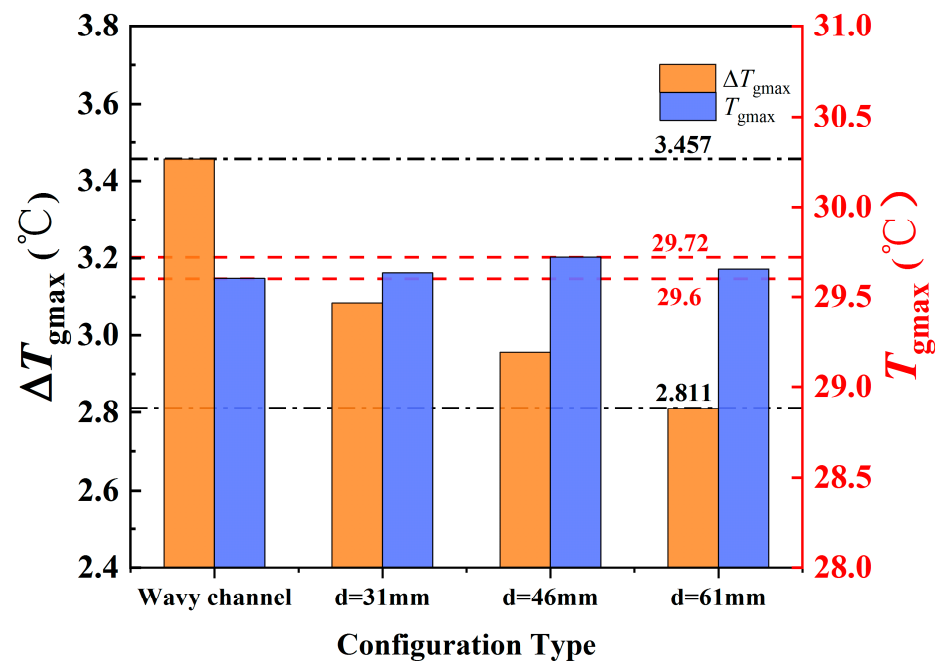


Figure 11. T_{gmax} and ΔT_{gmax} of battery module under different configurations.

3.3. Composite-Channel/PCM Design

Although the composite-channel design reduces the transverse temperature difference in the battery module, the longitudinal temperature difference in the battery height direction is still large, with a low temperature at the bottom of the battery and a high temperature at the top, as shown in Figure 9. This is because the heat transfers from the battery top to the coolant over a long distance with large thermal resistance, which results in slow heat dissipation and a high temperature at the top of the battery. Therefore, a composite-channel/phase change material (PCM) design is proposed in this section. PCM with a thickness of 2 mm is added to the top of each battery based on the composite-channel design, as shown in Figure 12. As shown in Figure 9, the maximum temperature of the battery is about 29 °C. Thus, RT27 paraffin wax was selected as the PCM, with a phase change temperature of 28 °C. When the temperature reaches the phase change temperature during battery discharge, the PCM will melt and quickly absorb the heat generated by the battery, which in turn reduces the maximum battery temperature. As shown in Figure 13, T_{max} per battery for the composite-channel/PCM design is significantly lower than that for the composite-channel design. The temperature difference per battery for the composite-channel/PCM design is also significantly improved due to the reduction in T_{max} . In addition, for the composite-channel/PCM design, the maximum temperature of the battery module is 29.22 °C, a reduction of 6.8% compared with the conventional straight-channel design (31.36 °C). Meanwhile, the maximum temperature difference in the battery module is 4.08 °C for the conventional straight-channel design, which is reduced by 41% for the composite-channel/PCM design (2.4 °C).

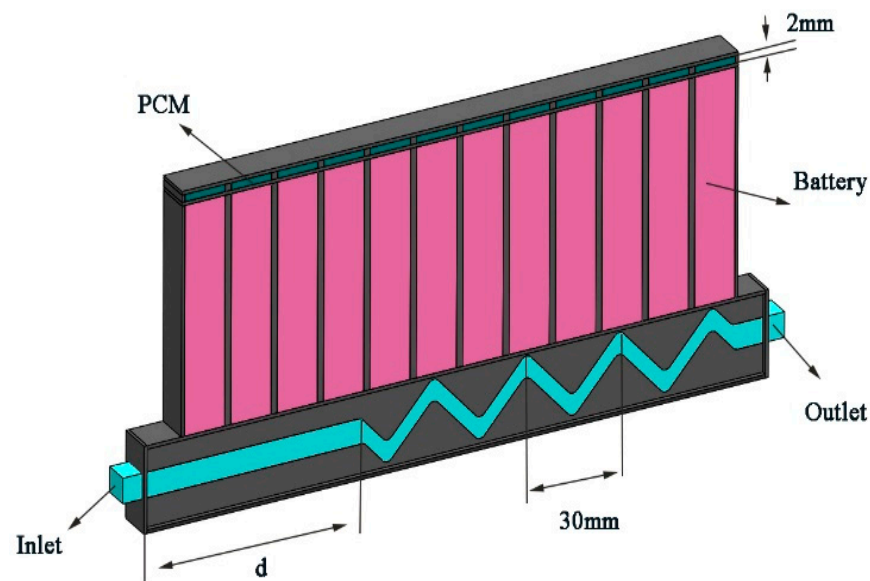


Figure 12. Schematic diagram of composite-channel/PCM design.

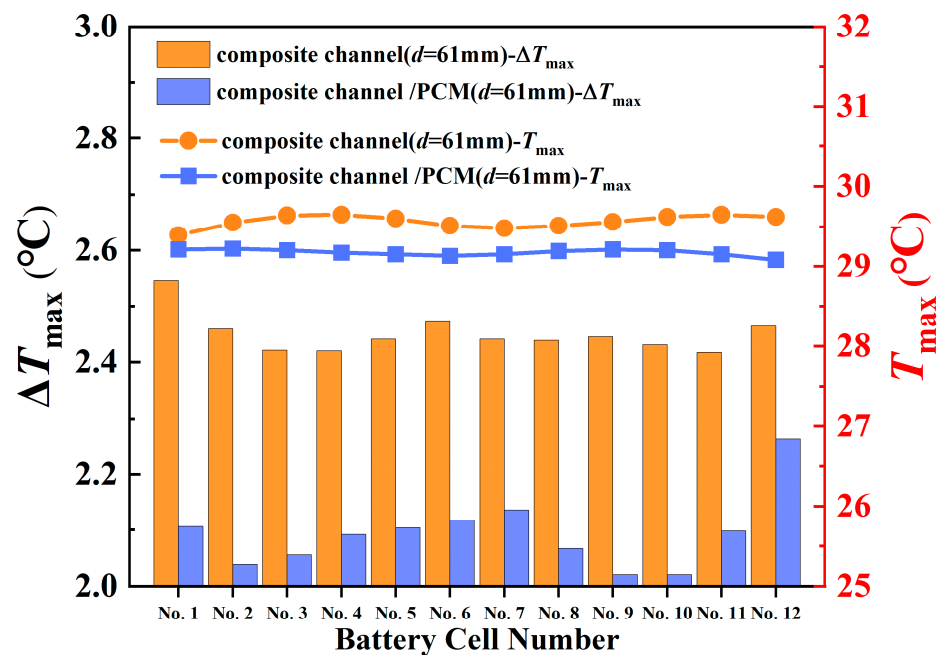


Figure 13. Temperature of composite-channel/PCM design.

4. Conclusions and Future Work

In this work, a wavy channel is proposed to strengthen the heat exchange capacity of the cold plate. To further reduce the temperature difference in the battery module in the coolant flow direction, a composite channel was designed. Finally, in order to reduce the temperature difference in the height direction of the battery, PCM is added to the top of the battery on the basis of the composite channel. The main conclusions obtained are as follows:

- (1) The wavy-channel design significantly strengthens the heat transfer between the battery bottom and the cold plate. The maximum battery module temperature T_{gmax} for the wavy channel is 29.61 °C, a reduction of 1.75 °C compared to the straight-channel design.
- (2) The composite-channel design significantly enhances the temperature uniformity between batteries.

- (3) The straight-channel length in the composite channel has a significant effect on the maximum temperature difference in the battery module.
- (4) Adding the PCM to the top of the battery significantly reduces the maximum temperature of the batteries, which in turn improves the temperature uniformity in the height direction of the battery.

Future work will include the optimization of the composite-channel/PCM design. There are many parameters influencing the cooling performance of the cold plate, such as the straight-channel length, cross-sectional shape, turning angle, wavelength and amplitude, and PCM thickness. Therefore, optimizing this many parameters of the composite-channel/PCM design is a challenge, which will be studied in the following work.

Author Contributions: Conceptualization, W.K.; Data curation, J.D.; Formal analysis, V.M. and H.X.; Investigation, X.L.; Methodology, X.L. and Y.S.; Software, H.X.; Writing—original draft, J.D.; Writing—review & editing, W.K. All authors have read and agreed to the published version of the manuscript.

Funding: This research was funded by the National Science Foundation of China, grant number 2179054. The APC was funded by 22179054.

Conflicts of Interest: The authors declare no conflict of interest.

References

1. Sarchami, A.; Najafi, M.; Imam, A.; Houshfar, E. Experimental study of thermal management system for cylindrical Li-ion battery pack based on nanofluid cooling and copper sheath. *Int. J. Therm. Sci.* **2022**, *171*, 1–10. [[CrossRef](#)]
2. Mo, C.; Zhang, G.; Yang, X.; Wu, X.; Li, X. A Battery Thermal Management System Coupling High-Stable Phase Change Material Module with Internal Liquid Cooling. *Energies* **2022**, *15*, 5863. [[CrossRef](#)]
3. Xu, Z.; Xu, J.; Guo, Z.; Wang, H.; Sun, Z.; Mei, X. Design and Optimization of a Novel Microchannel Battery Thermal Management System Based on Digital Twin. *Energies* **2022**, *15*, 1421. [[CrossRef](#)]
4. Chen, K.; Wu, W.; Yuan, F.; Chen, L.; Wang, S. Cooling efficiency improvement of air-cooled battery thermal management system through designing the flow pattern. *Energy* **2019**, *167*, 781–790. [[CrossRef](#)]
5. Wang, M.; Hung, T.-C.; Xi, H. Numerical Study on Performance Enhancement of the Air-Cooled Battery Thermal Management System by Adding Parallel Plates. *Energies* **2021**, *14*, 3096. [[CrossRef](#)]
6. Chen, Y.; Chen, K.; Dong, Y.; Wu, X. Bidirectional symmetrical parallel mini-channel cold plate for energy efficient cooling of large battery packs. *Energy* **2022**, *242*, 122553. [[CrossRef](#)]
7. Zhou, Y.; Wang, Z.; Xie, Z.; Wang, Y. Parametric Investigation on the Performance of a Battery Thermal Management System with Immersion Cooling. *Energies* **2022**, *15*, 2554. [[CrossRef](#)]
8. Jilte, R.; Afzal, A.; Panchal, S. A novel battery thermal management system using nano-enhanced phase change materials. *Energy* **2021**, *219*, 119564. [[CrossRef](#)]
9. Jin, X.; Duan, X.; Jiang, W.; Wang, Y.; Zou, Y.; Lei, W.; Sun, L.; Ma, Z. Structural design of a composite board/heat pipe based on the coupled electro-chemical-thermal model in battery thermal management system. *Energy* **2021**, *216*, 119234. [[CrossRef](#)]
10. Zhuang, Y.; Chen, T.; Chen, J.; Li, J.; Guan, M.; Chen, Y. Thermal uniformity performance of a hybrid battery thermal management system using phase change material and cooling plates arrayed in the manner of honeycomb. *Therm. Sci. Eng. Prog.* **2021**, *26*, 101094. [[CrossRef](#)]
11. Joula, M.; Dilibal, S.; Mafratoglu, G.; Danquah, J.O.; Alipour, M. Hybrid Battery Thermal Management System with NiTi SMA and Phase Change Material (PCM) for Li-ion Batteries. *Energies* **2022**, *15*, 4403. [[CrossRef](#)]
12. Yin, B.; Zuo, S.; Xu, Y.; Chen, S. Performance of liquid cooling battery thermal management system in vibration environment. *J. Energy Storage* **2022**, *53*, 105232. [[CrossRef](#)]
13. Qian, Z.; Li, Y.; Rao, Z. Thermal performance of lithium-ion battery thermal management system by using mini-channel cooling. *Energy Convers. Manag.* **2016**, *126*, 622–631. [[CrossRef](#)]
14. Rao, Z.; Zhang, X. Investigation on thermal management performance of wedge-shaped microchannels for rectangular Li-ion batteries. *Int. J. Energy Res.* **2019**, *43*, 3876–3890. [[CrossRef](#)]
15. Kong, W.; Zhu, K.; Lu, X.; Jin, J.; Ni, M. Enhancement of lithium-ion battery thermal management with the divergent-shaped channel cold plate. *J. Energy Storage* **2021**, *42*, 103027. [[CrossRef](#)]
16. Sheng, L.; Su, L.; Zhang, H.; Li, K.; Fang, Y.; Ye, W.; Fang, Y. Numerical investigation on a lithium ion battery thermal management utilizing a serpentine-channel liquid cooling plate exchanger. *Int. J. Heat Mass Transf.* **2019**, *141*, 658–668. [[CrossRef](#)]
17. Deng, T.; Zhang, G.; Ran, Y.; Liu, P. Thermal performance of lithium ion battery pack by using cold plate. *Appl. Therm. Eng.* **2019**, *160*, 114088. [[CrossRef](#)]
18. Ding, Y.; Ji, H.; Wei, M.; Liu, R. Effect of liquid cooling system structure on lithium-ion battery pack temperature fields. *Int. J. Heat Mass Transf.* **2022**, *183*, 122178. [[CrossRef](#)]

19. Xu, H.; Zhang, X.; Xiang, G.; Li, H. Optimization of liquid cooling and heat dissipation system of lithium-ion battery packs of automobile. *Case Stud. Therm. Eng.* **2021**, *26*, 101012. [[CrossRef](#)]
20. Xu, X.; Tong, G.; Li, R. Numerical study and optimizing on cold plate splitter for lithium battery thermal management system. *Appl. Therm. Eng.* **2020**, *167*, 114787. [[CrossRef](#)]
21. Chung, Y.; Kim, M.S. Thermal analysis and pack level design of battery thermal management system with liquid cooling for electric vehicles. *Energy Convers. Manag.* **2019**, *196*, 105–116. [[CrossRef](#)]
22. Li, Y.; Guo, H.; Qi, F.; Guo, Z.; Li, M.; Bertling Tjernberg, L. Investigation on liquid cold plate thermal management system with heat pipes for LiFePO₄ battery pack in electric vehicles. *Appl. Therm. Eng.* **2021**, *185*, 116382. [[CrossRef](#)]
23. Deng, T.; Ran, Y.; Zhang, G.; Yin, Y. Novel leaf-like channels for cooling rectangular lithium ion batteries. *Appl. Therm. Eng.* **2019**, *150*, 1186–1196. [[CrossRef](#)]
24. Alnaqi, A.A. Numerical analysis of pressure drop and heat transfer of a Non-Newtonian nanofluids in a Li-ion battery thermal management system (BTMS) using bionic geometries. *J. Energy Storage* **2022**, *45*, 103670. [[CrossRef](#)]
25. Li, B.; Wang, W.; Bei, S.; Quan, Z. Analysis of Heat Dissipation Performance of Battery Liquid Cooling Plate Based on Bionic Structure. *Sustainability* **2022**, *14*, 5541. [[CrossRef](#)]
26. Liu, X.; Sun, A.; Tian, C. Research on liquid cooling and heat dissipation of lithium-ion battery pack based on bionic wings vein channel cold plate. *Energy Storage Sci. Technol.* **2022**, *11*, 2266–2273.
27. Fan, Y.; Wang, Z.; Fu, T.; Wu, H. Numerical investigation on lithium-ion battery thermal management utilizing a novel tree-like channel liquid cooling plate exchanger. *Int. J. Heat Mass Transf.* **2022**, *183*, 122143. [[CrossRef](#)]
28. Ran, Y.; Su, Y.; Chen, L.; Yan, K.; Yang, C.; Zhao, Y. Investigation on thermal performance of water-cooled Li-ion cell and module with tree-shaped channel cold plate. *J. Energy Storage* **2022**, *50*. [[CrossRef](#)]
29. Mo, X.; Zhi, H.; Xiao, Y.; Hua, H.; He, L. Topology optimization of cooling plates for battery thermal management. *Int. J. Heat Mass Transf.* **2021**, *178*, 121612. [[CrossRef](#)]
30. Yan, S.; Wang, F.; Hong, J.; Sigmund, O. Topology optimization of microchannel heat sinks using a two-layer model. *Int. J. Heat Mass Transf.* **2019**, *143*. [[CrossRef](#)]
31. Guo, R.; Li, L. Heat dissipation analysis and optimization of lithium-ion batteries with a novel parallel-spiral serpentine channel liquid cooling plate. *Int. J. Heat Mass Transf.* **2022**, *189*. [[CrossRef](#)]
32. Pety, S.J.; Tan, M.H.Y.; Najafi, A.R.; Barnett, P.R.; Geubelle, P.H.; White, S.R. Carbon fiber composites with 2D microvascular networks for battery cooling. *Int. J. Heat Mass Transf.* **2017**, *115*, 513–522. [[CrossRef](#)]
33. Mallya, N.; Haussener, S. Buoyancy-driven melting and solidification heat transfer analysis in encapsulated phase change materials. *Int. J. Heat Mass Transf.* **2021**, *164*, 120525. [[CrossRef](#)]
34. Zhang, F.; Yi, M.; Wang, P.; Liu, C. Optimization design for improving thermal performance of T-type air-cooled lithium-ion battery pack. *J. Energy Storage* **2021**, *44*, 103464. [[CrossRef](#)]
35. Tete, P.R.; Gupta, M.M.; Joshi, S.S. Numerical investigation on thermal characteristics of a liquid-cooled lithium-ion battery pack with cylindrical cell casings and a square duct. *J. Energy Storage* **2022**, *48*, 104041. [[CrossRef](#)]
36. Wang, R.; Liang, Z.; Souri, M.; Esfahani, M.N.; Jabbari, M. Numerical analysis of lithium-ion battery thermal management system using phase change material assisted by liquid cooling method. *Int. J. Heat Mass Transf.* **2022**, *183*, 122095. [[CrossRef](#)]
37. Lamrani, B.; Lebrouhi, B.E.; Khattari, Y.; Kousksou, T. A simplified thermal model for a lithium-ion battery pack with phase change material thermal management system. *J. Energy Storage* **2021**, *44*, 103377. [[CrossRef](#)]